INSTITUTE OF PHYSICS PUBLISHING MEASUREMENT SCIENCE AND TECHNOLOGY

Meas. Sci. Technol. **18** (2007) 30–40 doi:10.1088/0957-0233/18/1/004

A particle filter approach for tomographic imaging based on different state-space representations

D Watzenig, M Brandner and G Steiner

Institute of Electrical Measurement and Measurement Signal Processing, Graz University of Technology, Kopernikusgasse 24, A-8010, Graz, Austria

E-mail: daniel.watzenig@tugraz.at

Received 19 January 2006, in final form 10 April 2006
Published 23 November 2006
Online at stacks.iop.org/MST/18/30

Abstract

In electrical capacitance tomography (ECT) the main focus is on the reconstruction of distinct objects with sharp transitions between different phases. Being inherently ill-posed, the reconstruction algorithm requires some sort of regularization to stabilize the solution of the inverse problem. However, introducing regularization may counteract the reconstruction of well-defined contours for grid-based methods. Level set propagation approaches which also rely on regularization are able to model sharp phase boundaries but suffer from high computational demands. In this contribution, two different state-space representations of closed contours based on B-splines and on Fourier descriptors are investigated. Both approaches allow us to describe the problem with only a small set of state-space variables. Regularization is incorporated implicitly which can be directly interpreted in the object domain as it relates to smooth contours. To solve the inverse problem, statistical inversion is performed by means of particle filtering providing the opportunity to conveniently incorporate prior information and to take measurement uncertainties into account. The proposed particle filter approach is compared to an extended Kalman filter realization in terms of complexity, computation time and estimation accuracy.

Keywords: electrical capacitance tomography, state-space representation, statistical inversion, particle filter

1. Introduction

Electrical capacitance tomography (ECT) is a non-invasive image-based technique that aims at estimating the permittivity distribution (ε_r-distribution) within closed objects [1–3]. Such objects are, for instance, pipelines in the oil industry or chambers and vessels in the production of food, chemicals and pharmaceuticals. ECT is able to provide information about internal states with low-cost requirements and is therefore well suited for industrial applications in order to determine process parameters such as void fraction or the status of completion of a mixing process. In ECT, voltage patterns are applied to the electrodes which are mounted along the circumference to acquire information about the interior of a closed object. The resulting inter-electrode capacitances which depend on the materials and their distribution inside the closed object are measured. Based on these measurements, the spatial material distribution is reconstructed. However, this reconstruction task is a nonlinear and severely ill-posed inverse problem [4, 5].

Many different algorithms have been developed and applied to tomographic tasks for two-phase flow fields in recent years with the objective of improving the image quality and reducing computational efforts in order to achieve real-time performance. The widely used deterministic reconstruction algorithms such as Gauss–Newton or Newton–Raphson try to fit the model to the data in a least-squares sense ignoring the presence of any noise sources. Furthermore, these

methods need some sort of regularization in order to stabilize the solution of the inverse problem. Regularization simply incorporates some *a priori* assumption on the material distribution and is implemented by adding a regularization term to the original cost functional to be minimized. The choice of the regularization parameter which controls the degree of regularization is crucial for the reconstruction task. Although many different methods to determine this parameter have been proposed in the literature (see, e.g., [6] for an overview) the key drawback is that there is no universally valid rule to adjust the regularization parameter up to now. Another drawback of regularization when using a sensor model based on the finite element method (FEM) is that it causes a blurring of phase transitions. However, in process tomography the main focus is on the identification of distinct objects with sharp boundaries (e.g., gas bubbles in oil). To overcome the problem of blurred images, different edge preserving methods for finite element based reconstruction techniques have been introduced. For example, the use of an auxiliary variable permits us to linearize the problem and to derive a deterministic algorithm based on alternate minimizations [7]. Due to the increased computational effort, this method is not applicable for real-time applications. Alternatively, various mesh grouping methods have been proposed to avoid blurred images (see e.g. [8]). The main disadvantage of these methods is that they rely on threshold levels which have to be identified by trial and error. A different possibility is to use the boundary element method (BEM) instead of the FEM to model the interior of the closed object. The inverse problem can then be solved, for example, by applying a numerical level set propagation approach [9]. The method inherently preserves object edges and implements a regularization based on the smoothness of the level set function. However, the drawbacks are the choice of the regularization parameter and the computational complexity due to a large number of model parameters.

To achieve sharp edges without increased computational effort it is reasonable to describe material boundaries by means of parametrized curves. Possible methods to represent the boundary of an object are the use of active contours [10] or the application of Fourier descriptors [11, 12]. These contour models are especially suitable for dynamic problems such as streaming fluids. Both methods use low-order state-space representations to incorporate model-based information into a boundary finding process for continuously deformable objects. Using these contour models the ECT problem can be solved by minimizing a quality criterion which is based on the difference between predicted and measured potentials. Including object dynamics these models can further be used to track objects. However, when reconstructing images from measured data, measurement noise as well as process noise cannot be neglected. To take both possible noise sources into account the inverse problem can be formulated as a statistical inference problem. The most natural approach is the application of Markov chain Monte Carlo (MCMC) methods (see, e.g., [13–16]). MCMC methods are very time consuming since the entire state-space is explored in terms of possible material distributions. MCMC methods are particularly useful to evaluate the estimated parameters with respect to sensitivity, bias, consistency and efficiency given measurements. Bayesian recursive estimators which are also able to incorporate stochastic state transitions and measurements are well suited especially for dynamic reconstruction tasks as is required in ECT. One such estimator is the Kalman filter (KF) [17]. In order to deal with the inherent nonlinearity of the measurement equations within the ECT framework, the extended Kalman filter (EKF) has been applied to tomographic tasks [18–20]. Its applicability is restricted to state vectors that are characterized by first-order and second-order statistical moments. This restriction still allows us to propagate Gaussian random variables. The occurrence of multiple object hypotheses—as frequently encountered during the reconstruction of dynamical set-ups—cannot be tackled properly by an algorithm restricted to unimodal state vector distributions. A less restrictive formulation of the Bayes principle based on sequential Monte Carlo (MC) simulations and a numerical approximation of non-Gaussian state densities is given by particle filters (PFs). In a direct comparison to the EKF, the PF offers the possibility of a non-approximate evaluation of the state transitions—even in the nonlinear case—and of multimodal state densities. Another appealing property of PFs is their straightforward incorporation of *a priori* information about the inner state of a dynamic system. On the downside, these advantages come at the cost of additional computations spent in the density approximation and the management of samples in state-space. The use of low-order state-space representations of closed contours enables the application of PF with considerably reduced computational effort.

This paper is structured as follows. Section 2 briefly describes the mathematical modelling of the ECT sensor. The representation of closed contours in state-space by means of B-splines and Fourier descriptors is addressed in section 3 followed by an introduction of the applied PF in section 4. The contour models are used for the reconstruction of two-phase test distributions based on synthetic data and compared in terms of the achievable reconstruction performance in section 5. The measurement set-up is outlined in section 6 followed by the evaluation of the proposed reconstruction algorithm with measured data for two experiments in section 7.

2. Mathematical model of the sensor

In ECT, the forward problem consists in determining the distribution of the electric scalar potential u_p for the active electrode pattern p and subsequently the electric field strength and the capacitance for a given permittivity distribution within the pipe. In each cycle of the applied electrode pattern, two electrodes are active, i.e. a certain potential is prescribed, while the remaining electrodes are floating—the measurement electrodes. The governing equation is a Laplace equation with boundary conditions,

$$\nabla \cdot (\varepsilon \nabla u_p) = 0 \tag{1}$$

$$u_p|_{\Gamma_0} = u_{0,p}, \tag{2}$$

where Γ_0 are the transmitting electrodes, where Dirichlet boundary conditions are prescribed. Figure 1(*a*) depicts the model of the sensor consisting of a tube with 16 electrodes

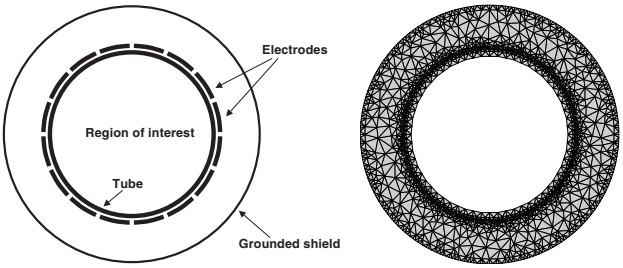

(*a*) Cross-section of the used ECT sensor

(*b*) Discretization of the pipe

Figure 1. Cross-section of the ECT sensor with 16 electrodes mounted on a pipe. The outer space is circumvented by a grounded conductive shielding. On the right, the discretization into linear finite elements of the electrodes, the tube and the outer space is depicted. Object boundaries in the region of interest are described by boundary elements.

equidistantly placed around the circumference and a conductive shield at ground potential at some distance from the tube outside the measurement volume. As neither the geometry nor the material values between the tube and the grounded shield change, it is advantageous to discretize the Laplace equation in this region with finite elements, whereas due to changing geometries and material values in the interior of the pipe, the BEM is applied [9]. Using the BEM in the region of interest increases the spatial resolution, since the discretization error due to finite elements is avoided. Figure 1(*b*) illustrates the discretization of the electrodes, the tube and the outer space with linear triangular finite elements while the interior of the pipe is one region for the BEM.

3. Representation of closed contours in state-space

Contours can be described as the boundaries between distinct regions with different properties. In the case of ECT, regions are distinguished by their distinct permittivity values. The contour $\mathcal{C}$ in $\mathbb{R}^2$ can be described by means of a vector-valued function $\mathbb{R} \to \mathbb{R} \times \mathbb{R} : s \mapsto \mathbf{c}(s)$ parametrized by $s \in [0, 1]$. $\mathcal{C}$ is *closed* if and only if $\mathbf{c}(0) = \mathbf{c}(1)$ and the Cartesian coordinates (x, y) of a point on the contour are given by the elements of $\mathbf{c}(s)$ as $\mathbf{c}(s) = (x(s), y(s))^T$.

Different representations of contours have been proposed in the literature (see, e.g., [12] for an overview). The common denominator of these contour models is the representation of $\mathcal{C}$ by as few parameters as possible while still meeting the requirements of the given application in terms of versatility. The set of parameters needed to fully describe the contour at any instance in time is referred to as the *state* of the model. Taking into account any evolution of the contour over time we can define the state-space representation of a contour by

$$\mathbf{x}_k = \mathbf{f}(\mathbf{x}_{k-1}, \mathbf{v}_{k-1}) \tag{3}$$

$$\mathbf{z}_k = \mathbf{h}(\mathbf{x}_k, \mathbf{w}_k), \tag{4}$$

where $\mathbf{f}(\cdot)$ represents the state transition of the state $\mathbf{x}$ from time $k-1$ to time k subjected to process noise which is modelled by $\mathbf{v}$. A measurement based on the current state $\mathbf{x}_k$ subjected to measurement noise $\mathbf{w}$ is modelled by $\mathbf{h}(\cdot)$. We are now able to formulate the reconstruction problem in the ECT as the problem of estimating the inner state (i.e. the current contour) of a dynamic system. In addition to approaches that reconstruct static set-ups, the use of dynamic models allows us to extend the algorithm towards dynamically changing set-ups.

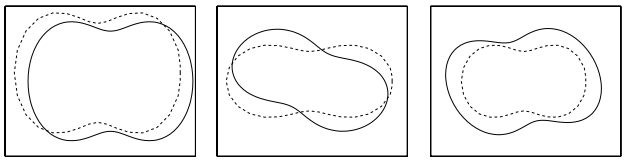

(*a*) (*b*) (*c*)

Figure 2. Geometric deformations of a B-spline subjected to an affine transformation (reference spline dashed): pure translation (*a*), rotation (*b*) and scaling and shear (*c*).

The different contour models have been designed in favour of distinct application requirements. In the following, we will introduce the B-spline model and Fourier descriptors and their respective applicability to the ECT problem.

3.1. B-spline representation

Using splines to represent contours requires us to approximate the true contour $\mathcal{C}$ by a linear combination of spline functions. While we have some freedom in choosing different spline functions, a commonly used set of basis functions $b_n(s)$ are bicubic functions, where $n = 0, \ldots, (N-1)$ denotes the current index in a representation using N basis functions. The resultant model is referred to as the *B-spline* representation of $\mathcal{C}$:

$$\hat{\mathbf{c}} = \begin{bmatrix} \mathbf{b}(s) & \mathbf{0} \\ \mathbf{0} & \mathbf{b}(s) \end{bmatrix} \begin{bmatrix} \mathbf{q}^x \\ \mathbf{q}^y \end{bmatrix} = \mathbf{U}(s)\mathbf{q}. \tag{5}$$

The vectors $\mathbf{q}^x = (x_0, x_1, \ldots, x_{N-1})^T$ and $\mathbf{q}^y = (y_0, y_1, \ldots, y_{N-1})^T$ denote the coordinates of the N *control points* and are used as weights for the respective basis functions. The vector $\mathbf{b}(s)$ is given by $\mathbf{b}(s) = (b_0(s), b_1(s), \ldots, b_{N-1}(s))^T$. Thus, a B-spline is represented by a vector $\mathbf{q}$ of size $2N$. In order to reduce the number of required parameters we introduce the shape-space representation of B-splines [10]. The shape-space of a contour is given by a linear transformation that maps a shape-space vector $\mathbf{x}$ to a spline vector $\mathbf{q}$ such that

$$\mathbf{q} = \mathbf{W}\mathbf{x} + \mathbf{q}_0, \tag{6}$$

where $\mathbf{q}_0$ represents a reference shape. Given that the dimension of the shape-space N_x is usually small compared to the size of the spline vector $N_q = 2N$, the shape-space representation results in a noticeable reduction of parameters. A B-spline now is represented by a reference B-spline $\mathbf{q}_0$ and a shape-space vector. The $N_q \times N_x$ shape matrix $\mathbf{W}$ enforces that deviations from the reference spline are restricted to geometrically meaningful deformations. As an example, the affine transformation in $\mathbb{R}^2$ has five degrees of freedom (dof) and can be represented in shape-space via the following transformation,

$$\mathbf{q} = \begin{pmatrix} \mathbf{1} & \mathbf{0} & \mathbf{q}_0^x & \mathbf{0} & \mathbf{0} & \mathbf{q}_0^y \\ \mathbf{0} & \mathbf{1} & \mathbf{0} & \mathbf{q}_0^y & \mathbf{q}_0^x & \mathbf{0} \end{pmatrix} \mathbf{x} + \mathbf{q}_0, \tag{7}$$

where the reference shape is given by $\mathbf{q}_0 = \left(\mathbf{q}_0^{xT}\mathbf{q}_0^{yT}\right)^T$. Figure 2 depicts a reference spline and its possible geometric

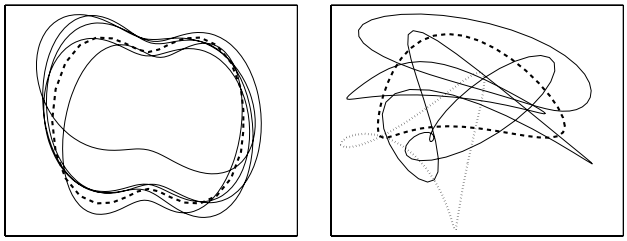

(*a*) (*b*)

Figure 3. Reference contours (dashed) and five random instances of the two contour models. (*a*) The B-spline representation is restricted to geometric deformations based on the shape matrix. (*b*) Varying the Fourier descriptors results in random contours not all of which have a physical meaning (see, e.g., the dotted contour).

deformations based on an affine shape matrix $\mathbf{W}$ as given by equation (7). Splines can be applied to problems where the reference contour $\mathbf{q}_0$ and its allowed geometric deformations are known. The restriction to a certain class of transformations in shape-space results in a high degree of regularization which can be utilized in the reconstruction process. In addition, splines lend themselves to stochastic shape representations by the introduction of random variables as elements within the shape-state vector $\mathbf{x}$. Figure 3(*a*) depicts a reference spline and five random instances of this model given that the state vector is comprised of Gaussian random variables. A major drawback of the B-spline representation is the restriction to geometric deviations of the reference shape that are covered by the transition model.

3.2. Fourier descriptors

An alternative representation of a closed contour $\mathcal{C}$ is based on the property that for any closed contour the coordinate functions $x(s)$ and $y(s)$ are periodic with a period $T = 1$. Therefore, we can approximate both functions using the Fourier series expansions to obtain

$$\hat{x}(s) = \frac{a_{x,0}}{2} + \frac{1}{2\pi}\sum_{n=1}^{N-1}(a_{x,n}\cos(2\pi ns) + b_{x,n}\sin(2\pi ns)) \quad (8)$$

$$\hat{y}(s) = \frac{a_{y,0}}{2} + \frac{1}{2\pi}\sum_{n=1}^{N-1}(a_{y,n}\cos(2\pi ns) + b_{y,n}\sin(2\pi ns)). \quad (9)$$

The approximation improves as the number of coefficients in the series representation increases. In this context, the Fourier series coefficients are referred to as *Fourier descriptors* of the contour.

As opposed to the B-spline representation, state transitions of Fourier descriptors in general do not correspond to any restricted family of geometric transformations of the underlying shape. Thus, the geometric regularization is less stringent than it is for the B-spline model. However, using Parseval's theorem the magnitude of the Fourier descriptors $m_{x,i}^2 = a_{x,i}^2 + b_{x,i}^2$ can be interpreted as the energy of the contour in the given frequency band. This contour model can, therefore, be used to apply a frequency-dependent convergence criterion as low-frequency components (i.e. the lower order Fourier descriptors) correspond to the coarse shape of the contour and high-frequency components (i.e. the higher order Fourier descriptors) correspond to details of the contour. Figure 3(*b*) indicates the variations in shape as a consequence of a stochastic Fourier descriptor model. As opposed to the B-spline case the Fourier descriptors can result in intersecting loops which cannot be used for the reconstruction of the objects under consideration in ECT.

4. Particle filter

According to the Bayesian approach the estimate of the unknown inner state $\mathbf{x}_k$ of a dynamic system at any time k is based on the totality of information present up to time k which is available through the measurements $\mathbf{z}_i, i = 1, \ldots, k$ corresponding to equation (4). In the following, a brief introduction to PFs is given; a detailed description can be found, for example, in [21–23]. Whereas for the KF the state is modelled using a multi-variate Gaussian distribution, the PF numerically approximates the potentially multimodal density of the state vector using the principle of *stochastic sampling*: a set of N points—the samples or particles $\mathbf{x}^{(m)}$—randomly chosen from the state-space and their respective weights $w^{(m)}$ can be used to represent a probability density function:

$$f_{\mathbf{x}}(\mathbf{x}) \approx \{\mathbf{x}^{(m)}, w^{(m)}\}_{m=1,\ldots,N}. \quad (10)$$

This approximation of the true density can be used to estimate moments such as the mean value. Assuming that the underlying process represents a first-order Markov chain, the state transition in equation (3) can be reformulated as conditional density $p(\mathbf{x}_k|\mathbf{x}_{k-1})$. Furthermore, the measurement model in equation (4) is expressed by $p(\mathbf{z}_k|\mathbf{x}_k)$ assuming independence between consecutive measurements. The PF keeps track of the current state estimate represented by $p(\mathbf{x}_k|\mathbf{Z}_k)$, where $\mathbf{Z}_k = \{\mathbf{z}_1, \ldots, \mathbf{z}_k\}$ denotes the history of measurements acquired up to time step k. In a recursive formulation, the PF performs two basic operations.

Prediction. At each time step the transition model is applied to obtain a state prediction $p(\mathbf{x}_k|\mathbf{Z}_{k-1})$ at time k using the Chapman–Kolmogorov equation

$$p(\mathbf{x}_k|\mathbf{Z}_{k-1}) = \int_{\Omega} p(\mathbf{x}_k|\mathbf{x}_{k-1})\, p(\mathbf{x}_{k-1}|\mathbf{Z}_{k-1})\, \mathrm{d}\mathbf{x}_{k-1}. \quad (11)$$

Numerically, the conditional density $p(\mathbf{x}_k|\mathbf{Z}_k)$ is represented using the sample set $S = \{\mathbf{x}_k^{(m)}, w_k^{(m)}\}$ where $m = 1, \ldots, N$. As indicated in figure 4, the prediction step comprises a deterministic drift and a stochastic diffusion process. The number of samples used to represent the state density is crucial for real-time operation. In general a trade-off between the quality of approximation and processing time is required. In order to maintain a good approximation of the true density using as few particles as possible a *resampling* step is added to the PF algorithm. While resampling is a necessity it also introduces considerable computational costs to the algorithm. Among different resampling strategies reported in the literature (see, e.g., [24–26] for a review) we apply the computationally efficient and numerically robust residual resampling [27]. The weights of the distinct samples in figure 4 are denoted by their respective size. Note that for the measurement step no weights are taken into account. It is only during the measurement that the samples obtain new weights based on their amplification or attenuation by the measurement model.

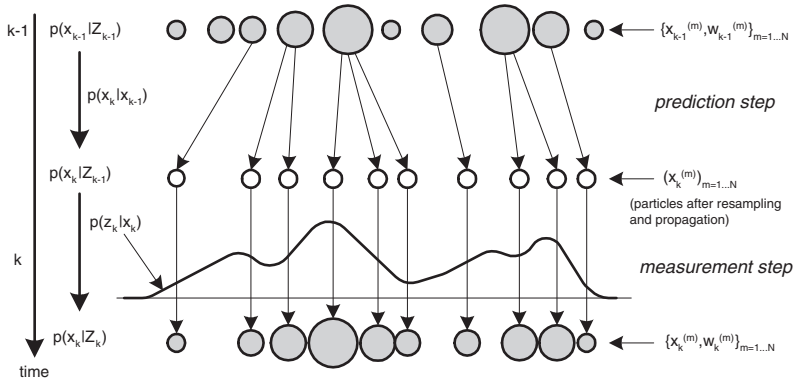

Figure 4. Principle of particle filtering. The old sample set at $k-1$ approximates the previous state density $p(\mathbf{x}_{k-1}|\mathbf{Z}_{k-1})$. The sizes of the particles reflect the weights that are assigned to them. After resampling and propagation through the state model, all particles have the same weights. However, samples with small weights have been removed, while samples with large weights have been replicated. In the measurement step, the measurement model $p(\mathbf{z}_k|\mathbf{x}_k)$ assigns new weights to each sample.

Measurement update. The second step within the PF iteration uses the measurement model $p(\mathbf{z}_k|\mathbf{x}_k)$ to estimate the posterior density $p(\mathbf{x}_k|\mathbf{Z}_k)$ by applying Bayes' theorem:

$$p(\mathbf{x}_k|\mathbf{Z}_k) = \frac{p(\mathbf{z}_k|\mathbf{x}_k)\,p(\mathbf{x}_k|\mathbf{Z}_{k-1})}{p(\mathbf{Z}_k)}. \tag{12}$$

In our application the measurement process is modelled by means of a multi-variate Gaussian distribution

$$p(\mathbf{z}_k|\mathbf{x}_k) \propto \exp\left\{-\tfrac{1}{2}(\mathbf{V}_m - \mathbf{z}_k)^T \Sigma^{-1}(\mathbf{V}_m - \mathbf{z}_k)\right\}, \tag{13}$$

where $p(\mathbf{z}_k|\mathbf{x}_k)$ denotes a likelihood function and $\mathbf{V}_m$ is the vector of measured electrode potentials. This assumption which greatly simplifies the measurement update has to be validated for the given measurement set-up (see section 6). The output of the PF algorithm is a set of samples which is used to approximate the posterior distribution. From these samples, any point estimate of the system state such as the maximum *a posteriori* estimate, the maximum likelihood estimate, the median and the expected value of the state can be calculated. In this work, the expected value given by

$$\hat{\mathbf{x}}_k = E\{\mathbf{x}_k|\mathbf{Z}_k\} \approx \sum_{m=1}^{N} w_k^{(m)} \mathbf{x}_k^{(m)} \tag{14}$$

is chosen to characterize the output of the PF. As a main advantage of the PF over the EKF the resultant posterior distribution gives information about confidence intervals of the calculated estimates in the case of non-Gaussian state and noise distributions as well as summary statistics about parameters of interest.

5. Validation of the method

In order to validate the proposed approach two different simulation experiments on two-phase flow fields are performed. The simulations were carried out using a B-spline representation with a circular reference contour and a five dof shape vector. For the Fourier descriptor approximation $2(2N+1) = 10$ Fourier coefficients were used. The state transition (3) is assumed to be a random walk process, i.e. the change between two consecutive states is only influenced by stochastic diffusion—the process noise. In order to improve the convergence behaviour of the PF the state vector $\mathbf{x}$ is segmented into the translation $\mathbf{x}_\mathcal{T}$ and the deformation part $\mathbf{x}_\mathcal{D}$ where different process noise levels for each part are assumed,

$$\mathbf{x} = \left(\mathbf{x}_\mathcal{T}^T, \mathbf{x}_\mathcal{D}^T\right)^T. \tag{15}$$

A standard deviation of 0.5×10^{-3} is assumed for the process noise which corresponds to the translational part and a standard deviation of 2×10^{-4} is prescribed for the noise level which is associated with the deformation part of the dynamic contour. The standard deviation of the measurement noise for the numerical experiments is set to 2×10^{-5} V. The first test case illustrates the convergence behaviour of the applied PF when the B-spline representation is used to describe the boundaries of a gas bubble ($\varepsilon_r = 1$) in oil ($\varepsilon_r = 2$). The PF is initialized with 16 particles of circular shape that are uniformly distributed over the cross-section of the pipe. The reference object, i.e. the gas bubble to be located, has an elliptical form. It is indicated as a bold dashed contour in figure 5. The grey contours show the single particles, while the bold black object stems from the expectation of the posterior state density. The situation after the second iteration of the PF is depicted in figure 5(*a*), while figure 5(*b*) shows the state after iteration 4. After only four iterations almost all particles are

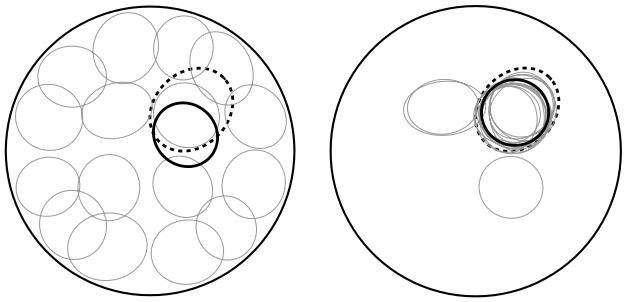

(*a*) Iteration 2 (*b*) Iteration 4

Figure 5. Evolution of the PF with B-spline contour model for a gas bubble immersed in oil. The plots show all particles (thin grey contours) and the expectation of the posterior state density (bold black contour) in comparison to the true bubble (bold dashed contour) after iterations 2 and 4, respectively.

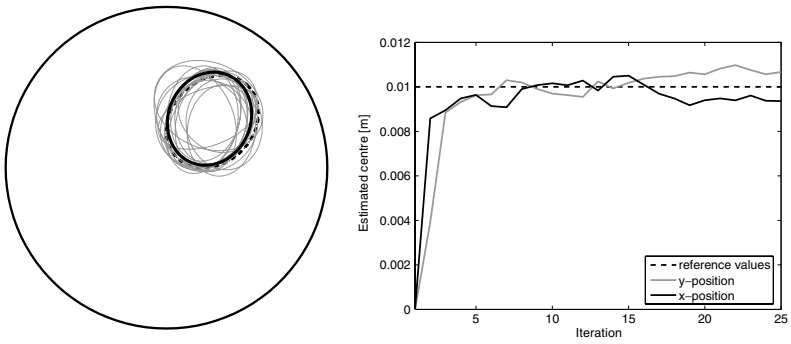

(*a*) Iteration 25 (*b*) Estimated centre of the bubble

Figure 6. Estimation result of the PF with B-spline contour representation after 25 iterations. The estimated shape (bold line) is almost congruent with the reference shape (dashed line). The chart on the right illustrates the progression of the estimated centre coordinates where the dashed line corresponds to the reference position ($x = y = 0.01$ m). The centre of the pipe is the point of origin.

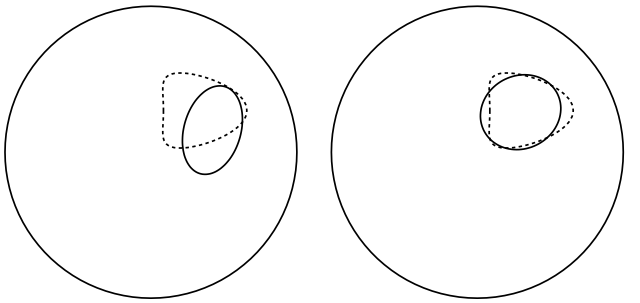

(*a*) Iteration 2 (*b*) Iteration 30

Figure 7. Contour estimates of the PF with B-spline contour model for a triangle-like gas bubble at different iterations. The dashed contour indicates the true bubble shape. The used model does not allow an exact match of the true shape.

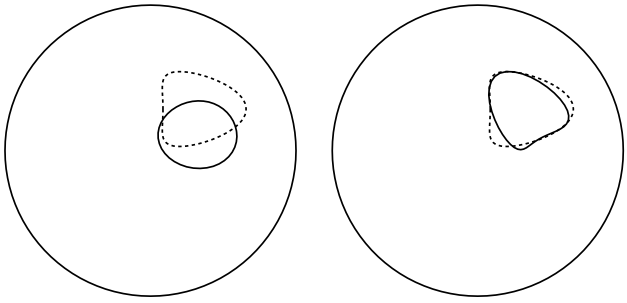

(*a*) Iteration 2 (*b*) Iteration 30

Figure 8. Contour estimates of the PF with Fourier coefficient contour model for a triangle-like gas bubble at different iterations. The dashed contour indicates the true bubble shape. The used model would allow us to exactly match the true shape, but it cannot be achieved due to the ill-posedness of the problem.

contracted to the right position. However, the size and the shape still have to be adjusted. The estimation result after 25 iterations is plotted in figure 6(*a*). There are still particles with wrong position, size and shape originating from the stochastic sampling, but the associated weights of these particles are low. The expectation of the state density approximates the true bubble reasonably well. The progression of the estimated centre is illustrated in figure 6(*b*). It can be seen that after about five iterations the estimate for the centre is within a tolerance band where it remains over the iterations. The second experiment consists of a gas bubble resembling a triangular shaped gas inclusion in oil, shown as bold dashed contour in figure 7. Such a shape cannot be emulated with splines based on an affine transformation of a circular reference shape, as used in our work. The performance of the PF with spline-based contour model is illustrated in figure 7, where the expectations of the posterior distribution at two different iterations are compared with the true bubble. The filter is initialized with 30 particles to allow for a better coverage of the true object shape. The filter estimates after 2 and 30 iterations are shown in the figure. Similar to the first example shown in figure 5 the true object position can be reached after a few filter iterations, while a reasonable approximation of the reference shape takes more iterations. The estimate of iteration 30 is depicted in figure 7(*b*), where the shape of the spline contour is an ellipsoidal approximation of the true bubble. A better match is not achievable with the used contour model. However, the filter with B-spline model is able to produce robust approximations of complex contours due to the low number of hidden states. The performance of the PF with a second-order Fourier descriptor shape model on the same reconstruction problem is illustrated in figure 8. The evolution of the shape estimates is very similar to that of the spline-based filter. In contrast to the spline model, the Fourier descriptor model is in principle capable of exactly matching the reference contour. However, the ECT problem is ill-posed, i.e. the sensitivity of the measured electrode potentials with respect to higher order contour details is very poor. Therefore the power of the Fourier descriptor model cannot be exploited in the present application. As can be seen from figure 8(*b*), the shape reconstruction is qualitatively similar to the spline-based results. To further study the correlation between the sensitivity of the forward problem and the reconstruction quality, the PF with Fourier descriptors is applied to a third test case. The reference bubble is a triangle with sharp edges and a dent on one side. The edges cannot be reconstructed if a gas bubble with a relative permittivity $\varepsilon_r = 1$ is assumed. However, in the performed experiment the bubble is assumed to consist of

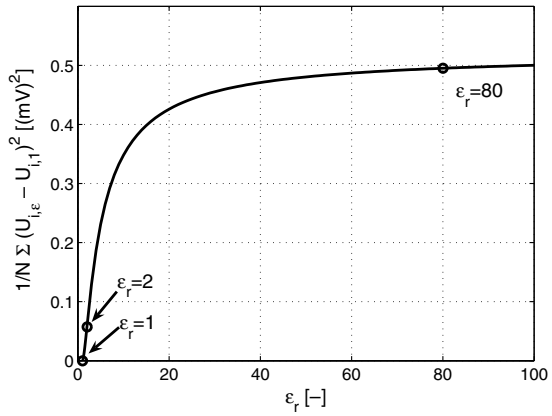

Figure 9. Mean squared deviation of the simulated electrode potentials for a small disturbance of varying permittivity in the centre of the pipe in comparison to the homogeneous case with a constant relative permittivity of 1. The sensitivity of the electrode potentials initially increases with rising permittivity, but strong saturation occurs for relative permittivity values above 10.

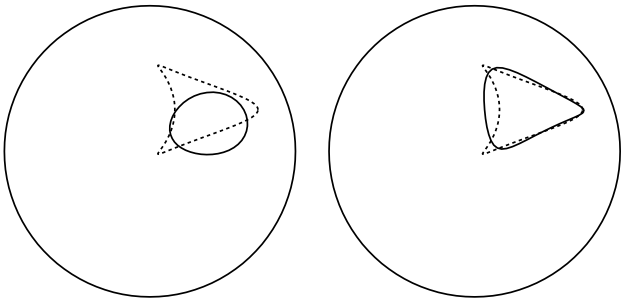

(*a*) Iteration 2 (*b*) Iteration 40

Figure 10. Contour estimates of the PF with Fourier contour model for a triangle-like water bubble with sharp edges at different iterations. The dashed contour indicates the true shape. Due to the high permittivity contrast between water and oil the details of the true contour can be better matched than for gas bubbles.

water with $\varepsilon_r = 80$. This results in a stronger contrast between the bubble and the background medium and therefore in a higher sensitivity of the forward problem to fine details in the problem region. Figure 9 gives an indication of the sensitivity of the electrode potentials to a small inclusion as a function of the permittivity contrast of the perturbation. A circular inclusion with a diameter of 5 mm placed in the centre of the pipe and with a varying relative permittivity has been simulated against a background with $\varepsilon_r = 1$. The figure shows the mean squared deviation of the simulated electrode potentials with respect to the unperturbed case (empty pipe). The deviation rises steeply with increasing permittivity. However, the curve quickly flattens above a relative permittivity of 10. The strongest contrast with respect to the electrode potentials can be attained with permittivities higher than 40. It is rather low in comparison for small permittivities. The mean squared deviation at $\varepsilon_r = 2$, for example, is only 12% of the value achievable with $\varepsilon_r = 80$. The resultant filter performance in the high-contrast case is illustrated in figure 10. The edges and the straight lines of the reference contour can be matched much better than for gas bubbles.

6. Measurement set-up

6.1. General description

Figure 11 illustrates the ECT measurement set-up. Our ECT sensor consists of a PVC pipe with a diameter of 75 mm with 16 electrodes mounted equidistantly around the circumference. In order to apply a two-dimensional imaging technique and to overcome field inhomogeneities at the edges of electrodes, the electrodes must have a certain length compared to their width. In fact, the electrodes are designed to a size of 70 mm × 7.3 mm. A grounded copper shielding is used to avoid stray capacitances. To achieve a good overall sensitivity within the entire cross-section of the pipe, a predefined sequence of excitation voltages is applied to the electrodes. Each measurement cycle consists of eight individual measurements. During each such measurement two electrodes are active (i.e. driven to $U_B = \pm 2.5$ V) while the remaining 14 electrodes are floating and switched to receiving mode. The resulting potentials on the receiving electrodes depend on the material distribution, i.e. the dielectric permittivities, inside the pipe. The signals captured by each receiving electrode are amplified, bandpass filtered, and passed on to a peak detector. Prior to A/D conversion the logarithm of each signal is determined in the analogue domain ensuring a highly dynamic signal acquisition and thus the coverage of a wide range of permittivities. The control of the sensor is performed by a dSPACE prototyping system. A set of measured potentials which is used to reconstruct a two-dimensional permittivity distribution of the cross-section of the pipe is depicted in figure 12.

6.2. Measurement noise analysis

Both the sensor front-end and the subsequent signal processing introduce noise sources to the measurement process. As indicated in section 4 the particle filter updates can be simplified based on the assumption of Gaussian measurement likelihoods. In order to validate this assumption the distribution of the measured potentials has been examined based on $N = 50\,000$ repeated measurements for an empty pipe. Figure 13 depicts the normalized quantile plot and the histogram of the received potential of electrode 9. This particular electrode is in good agreement with the Gaussian noise assumption. However, imperfections in the hardware set-up such as signal coupling (crosstalk between transmitter and receiver) between electrodes and saturation effects in the analogue front-end result in potential distributions that deviate from the Gaussian assumption. An example measured at electrode 12 is shown in figure 14. In both cases electrodes 3 and 13 have been used as transmitting electrodes. Similar to electrode 12 deviations from the Gaussian distribution have been carried out for electrodes 2, 4 and 11. From these results one can gather that there is obviously crosstalk between the transmitting electrode and its adjacent electrodes yielding a one-sided longer tailed Gaussian distribution towards smaller amplitudes of the electric potential. This asymmetry gives rise to a bias of the measured electric potentials at adjacent electrodes. However, the small amplitude of the bias error does not affect the convergence behaviour of the reconstruction algorithm (cf section 7).

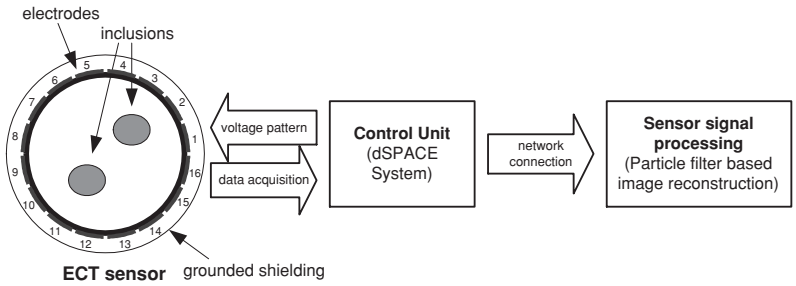

Figure 11. Block diagram of the measurement set-up consisting of the ECT sensor, a control unit and the sensor signal processing to obtain images of the cross-sectional permittivity distribution of the pipe based on particle filtering.

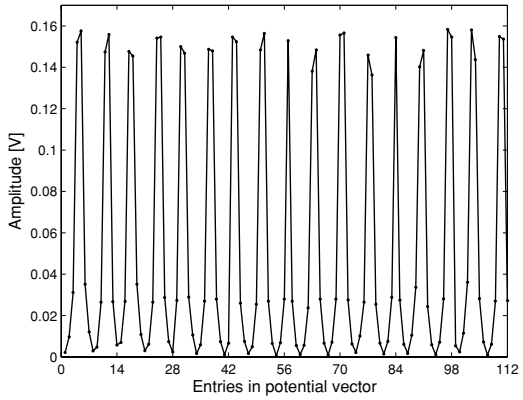

Figure 12. Acquired potential vector after rectification, peak detection and A/D conversion with a resolution of 16 bits. The size of the vector is 112 corresponding to the electrode switching pattern 14×8.

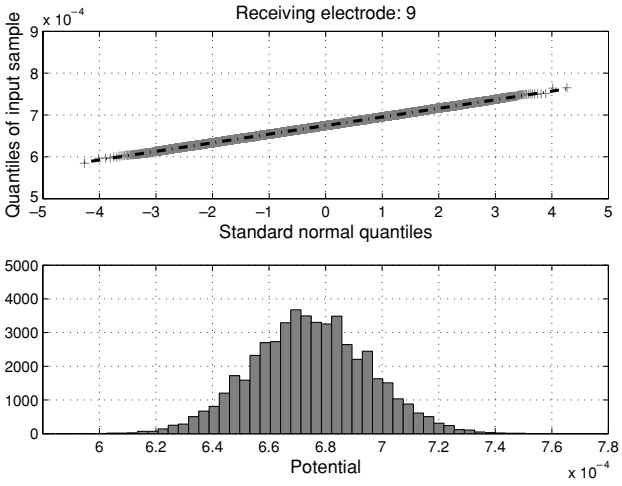

Figure 13. Normalized quantile plot (top) and histogram (bottom) of the potentials measured at electrode 9 during $N = 50\,000$ repeated measurements. The potential distribution meets the Gaussian assumption.

In summary, the majority of the measured electrode potentials exhibit noise properties that can be properly modelled by additive white Gaussian noise as assumed by our PF implementation. Deviations from this assumption are minor and still result in satisfactory convergence properties of the reconstruction algorithm.

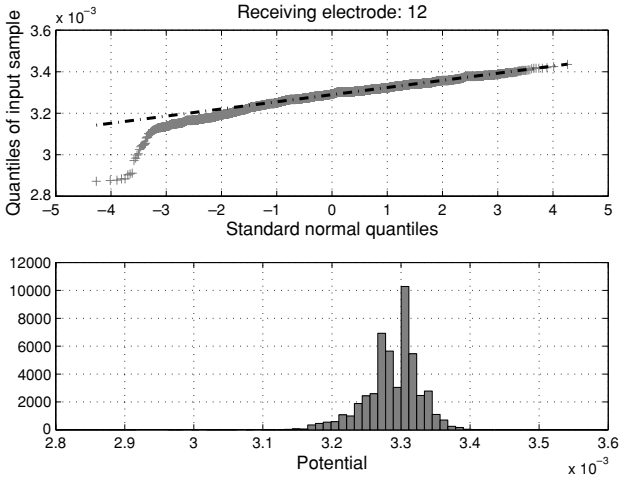

Figure 14. Distribution of the $N = 50\,000$ measured potentials of electrode 12. Due to crosstalk between transmitting electrode 13 and adjacent electrodes (12 and 14) a bias is introduced and hence the distribution deviates from the Gaussian assumption which is clearly visible in the normalized quantile plot (top) and the asymmetric histogram of the potentials (bottom).

7. Results with measured data

In order to present the applicability of the proposed approach for measured data the following two static experiments have been performed:

- PVC rod ($\varepsilon_r \approx 3.5$) with a diameter of 20 mm placed inside the air-filled pipe (cf figure 15).
- Half of a 50 mm PVC rod ($\varepsilon_r \approx 3.5$) placed inside the air-filled pipe (cf figure 16).

The first experiment leads to a circle in the case of the cross-sectional imaging technique while the second experiment yields a semi-circle. Based on the two measured data sets the proposed PF approach and the EKF are applied to invert the data given measurement noise. Both algorithms are subsequently compared in terms of complexity, computation time and efficiency. The implementation of an EKF for ECT in order to estimate phase boundaries is discussed in [28]. Figure 15(*b*) depicts the reconstruction results for both algorithms. The bold black line denotes the estimated contour after 20 iterations using the PF approach while the dashed grey shape corresponds to the result of the EKF after 60 iterations. Both reconstruction algorithms use the B-spline state-space representation of the closed contour. For

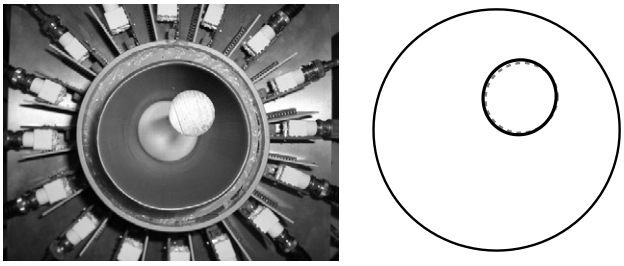

(*a*) (*b*)

Figure 15. Result of the PF- and the EKF-based image reconstruction using the B-spline contour model for the PVC rod in air. (*a*) Top view of the sensor. (*b*) Reconstructed images using the B-spline model. The black bold contour indicates the result of the PF after 20 iterations, the dashed grey contour denotes the result of the EKF-based reconstruction after 60 iterations. Applying the Fourier contour model yields the same result.

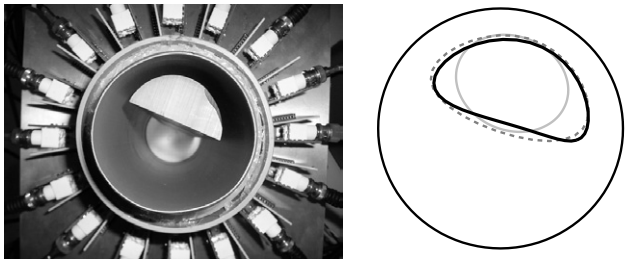

(*a*) (*b*)

Figure 16. Results of the PF- and the EKF-based image reconstruction approaches. (*a*) Top view of the sensor. (*b*) Reconstructed images. The black bold contour represents the estimated contour using the PF approach while the dashed grey shape corresponds to the estimated contour using the EKF. Both reconstruction approaches are based on the Fourier descriptor contour model. In addition, the PF-based contour estimation using the B-spline model is depicted (bold light grey shape). The centre of mass is reconstructed reasonably well while the reconstruction of the contour fails due to the restricted class of possible deformations of the B-spline model.

the circular PVC inclusion both state-space approaches—the Fourier descriptors and the B-spline model—lead to the same result. The second experiment treats a more complex shape. Due to the fact that the shape matrix is restricted to a certain class of deformations, namely translation, rotation, scaling and shear, the B-spline model is not able to match the semi-circle properly. On the other hand, the truncated Fourier model of order 10 fits the PVC object in both position and shape very well. It takes 60 iterations for the EKF and 25 iterations for the PF to estimate the contour of the unknown object. Figure 16(*b*) depicts the estimation results for both approaches. In both cases the Fourier contour model is applied. The bold black shape is associated with the PF while the dashed grey contour corresponds to the estimation result using the EKF. In addition, the reconstruction result using the B-spline model in combination with the PF is presented. As a matter of fact, the contour model is not able to estimate the semi-circle-shaped contour. However, the centre of mass is reconstructed reasonably well. Table 1 summarizes the differences between EKF and PF in terms of required iterations, complexity and computation time. The

Table 1. EKF and PF compared for one complete inversion using measured data.

Comparable quantities	EKF	PF
Number of iterations i	60	20
Number of particles n	–	20
Solved forward problems	60	$i \times n = 400$
Number of calculated Jacobians	60	–
Computation time	47.047 s	147.375 s

EKF solves the forward map once in each iteration while the PF requires the solution of $i \times n$ forward problems in order to invert the measured data set. Consequently, the contour estimation using the PF takes three times longer than the application of an EKF. The estimation results are carried out on a personal computer (AMD Athlon 1.73 GHz, 1 GB RAM). In the present work, the EKF is initialized with a circular-shaped contour in the centre of the pipe. If the initial state is far away from the target the EKF tends to diverge even if the number of iterations is increased. The PF is initialized with 20 particles which are uniformly distributed throughout the cross-section of the pipe. As discussed in section 5 it takes about five iterations for the PF to concentrate the involved particles around the target. Furthermore, there is no need to calculate the Jacobian—the derivatives of the boundary elements with respect to their normal directions. Consequently, PFs are applicable for highly nonlinear forward maps or in cases where singularities occur in the Jacobian. However, the main advantage of applying a PF to solve the inverse ECT problem is that the solution is a probability distribution—the posterior distribution—rather than a single point estimate. From this posterior distribution any estimates such as the median and the maximum *a posteriori* estimate for the unknown parameters can be calculated and their reliability by considering confidence intervals and marginal densities can be investigated.

Table 2 summarizes different quantities of interest such as estimated area and circumference of the target and obtained void fraction averaged over five independent image reconstructions in order to discuss the efficiency of the PF compared to the EKF. Both reconstruction algorithms use the Fourier descriptor model to represent a closed contour in the state-space. Due to the absence of a reference measurement system the position of the targets cannot be used as a reconstruction quality parameter. The estimation results for the simple circular contour are quite similar between EKF and PF. Once the EKF and the PF are in equilibrium, i.e. the difference between measured and calculated electric potentials is below a certain level ($<$10 mV), the collected data for area are averaged. PF-based estimated area and estimated circumference are closer to the true values compared to the EKF yielding better results in void fraction. The relative error in void fraction is reported to be 3.5 times smaller than that using the EKF. However, due to the property of the PF to explore the state-space in each iteration using 20 particles more stochastic variability is incorporated into the estimation process yielding improved results for the complex-shaped contour. In fact, the relative error in void fraction is about 0.3% which is 6.5 times smaller than the remaining error using the EKF.

Table 2. Reconstruction results of EKF and PF compared.

Quantities	True values	Results by EKF	Results by PF
Area of circle (m^2)	3.1416×10^{-4}	3.262×10^{-4}	3.109×10^{-4}
Circumference of circle (m)	0.0628	0.0714	0.0672
Void fraction of circle (%)	8.1633	8.4761	8.0786
Relative error in void fraction of circle (%)	–	3.8327	1.0375
Area of semi-circle (m^2)	9.8175×10^{-4}	1.0×10^{-3}	9.7895×10^{-4}
Circumference of semi-circle (m)	0.1285	0.1187	0.1164
Void fraction of semi-circle (%)	25.5102	25.9845	25.4374
Relative error in void fraction of semi-circle (%)	–	1.8592	0.2852

Table 3. Posterior variability for the first experiment.

Quantities	Mean	Standard deviation
x-coordinate of centre of mass (m)	8.000×10^{-3}	1.997×10^{-4}
y-coordinate of centre of mass (m)	1.328×10^{-2}	1.249×10^{-4}
Area (m^2)	2.269×10^{-4}	6.660×10^{-7}
Circumference (m)	5.498×10^{-2}	7.948×10^{-5}

Table 4. Posterior variability for the second experiment.

Quantities	Mean	Standard deviation
x-coordinate of centre of mass (m)	4.883×10^{-3}	1.463×10^{-4}
y-coordinate of centre of mass (m)	9.691×10^{-3}	4.318×10^{-5}
Area (m^2)	9.054×10^{-4}	2.263×10^{-5}
Circumference (m)	1.172×10^{-1}	1.023×10^{-3}

An important feature of particle filtering is the possibility of calculating different statistics from the resultant sample set. The posterior variability in shape, position, circumference and estimated area at iteration 20 for the first experiment is summarized in table 3. Table 4 shows summary statistics for the second experiment after iteration 25 considering 20 particles.

8. Conclusions

In this contribution, a novel approach to represent closed contours in state-space for two-phase fields in ECT is proposed. The boundary of the object to be located is modelled by means of a parametrized curve. Two different approaches—a description with B-splines and a Fourier representation—are investigated and compared. In order to take measurement uncertainties into account the inverse problem is recast in the form of statistical inference and solved numerically by means of particle filtering. Regularization is implicitly achieved which can be directly interpreted in the object domain as it relates to smooth contours. Due to the restriction to a certain class of transformations in shape-space B-splines are only applicable to problems where the reference contour and its allowed geometric deformations are known. In contrast to B-spline contour models Fourier descriptors are able to model more complex contours. While the B-spline model fails to properly model shapes containing higher frequency parts the application of a second-order Fourier model enables the reconstruction of corners and indentations within such shapes. The proposed PF approach to solve the nonlinear inverse ECT problem has been validated for both contour models using simulated and measured data. By setting up two different static experiments corresponding to a circular and a semi-circular inclusion with a known constant and homogeneous permittivity in an air-filled pipe the applicability of the contour models has been investigated. The PF approach has been compared to an EKF reconstruction algorithm in terms of complexity, computation time and accuracy of the obtained estimates. As a result, the EKF is about three times faster than the PF, however, the estimated parameters such as area, circumference and void fraction are closer to their true values using the PF due to the stochastic variability incorporated by the PF algorithm.

Since this first approach is based only on static experiments, future work will focus on simultaneously tracking a moving object inside the pipe and recovering its shape. Furthermore, the reconstruction of multiple inclusions and the extension of the state-space vector in order to estimate shape parameters as well as absolute permittivity values within two-phase flow scenarios should be addressed.

References

[1] Scott D M and McCann H 2005 *Process Imaging and Automatic Control* (Boca Raton, FL/London: CRC Press/Taylor and Francis Group)

[2] Beck M S, Dyakowski T and Williams R A 1998 Process tomography—the state of the art *Trans. Instrum. Meas. Control* **20** 163–77

[3] York T 2001 Status of electrical tomography in industrial applications *J. Electron. Imaging* **10** 608–19

[4] Tarantola A 2005 *Inverse Problem Theory and Methods for Model Parameter Estimation* (Philadelphia, PA: SIAM)

[5] Bertero M and Boccacci P 1998 *Inverse Problems in Imaging* (Philadelphia, PA: Institute of Physics Publishing)

[6] Hansen P C 1998 *Rank-Deficient and Discrete Ill-Posed Problems* (Philadelphia, PA: SIAM)

[7] Charbonnier P, Blanc-Feraud L, Aubert G and Barlaud M 1997 Deterministic edge-preserving regularization in computed imaging *IEEE Trans. Image Process.* **6** 298–311

[8] Kim K Y, Kim B S, Kim M C, Kim S, Lee Y J, Jeon H J, Choi B Y and Vauhkonen M 2004 Electrical impedance imaging of two-phase fields with an adaptive mesh grouping scheme *IEEE Trans. Magn.* **40** 1124–7

[9] Kortschak B and Brandstätter B 2004 A FEM–BEM approach using level-sets in tomography *COMPEL—Int. J. Comput. Math. Electr. Electron. Eng.* **24** 591–605

[10] Blake A and Isard M 1998 *Active Contours* (London: Springer)

[11] Jeon H J, Kim J H, Choi B Y, Kim K Y, Kim M C and Kim S 2005 Electrical impedance imaging of binary mixtures with boundary estimation approach based on multilayer neural network *IEEE Sensors J.* **5** 313–20

[12] Sonka M, Hlavac V and Boyle R 1999 *Image Processing, Analysis, and Machine Vision* 2nd edn (Pacific Grove, CA: Brooks/Cole)
[13] Kaipio J P, Kolehmainen V, Somersalo E and Vauhkonen M 2000 Statistical inversion and Monte Carlo sampling methods in electrical impedance tomography *Inverse Problems* **16** 1487–522
[14] Kaipio J P and Somersalo E 2004 *Statistical and Computational Inverse Problems* (*Applied Mathematical Sciences* vol 160) (New York: Springer)
[15] Martin T and Idier J 1998 A FEM-based nonlinear MAP estimator in electrical impedance tomography *Proc. Int. Conf. on Image Processing (Santa Barbara, CA, USA, 1997)* vol 2, pp 684–7
[16] Aykroyd R G, Cattle B A and West R M 2005 Boundary element method and Markov chain Monte Carlo for object location in electrical impedance tomography *Proc. 5th Int. Conf. on Inverse Problems: Theory and Practice (Cambridge, UK)*
[17] Kalman R E 1960 A new approach to linear filtering and prediction problems *J. Basic Eng.* **82** 35–45
[18] Vauhkonen M, Karjalainen P A and Kaipio J P 1998 A Kalman filter approach to track fast impedance changes in electrical impedance tomography *IEEE Trans. Biomed. Eng.* **45** 486–93
[19] Watzenig D, Steiner G and Brandstätter B 2004 Managing noisy measurement data by means of statistical parameter estimation in electrical capacitance tomography *Proc. 11th Int. IGTE Symp. on Numerical Field Calc. in Electrical Eng. (Graz, Austria)* pp 196–201
[20] Kim K Y, Kim B S, Kim M C and Kim S 2004 Dynamic inverse obstacle problems with electrical impedance tomography *Math. Comput. Simul.* **66** 399–408
[21] Arulampalam M S, Maskell S, Gordon N J and Clapp T 2002 A tutorial on particle filters for online nonlinear/non-Gaussian Bayesian tracking *IEEE Trans. Signal Process.* **50** 174–88
[22] Kotecha J H and Djuric P M 2003 Gaussian particle filtering *IEEE Trans. Signal Process.* **51** 2592–601
[23] Liu J S and Chen R 1998 Sequential Monte Carlo methods for dynamic systems *J. Am. Stat. Assoc.* **93** 1032–44
[24] Doucet A, de Freitas N and Gordon N J 2001 *Sequential Monte Carlo Methods in Practice* (New York: Springer)
[25] Gordon N J, Salmond D J and Smith A F M 1993 Novel approach to nonlinear/non-Gaussian Bayesian state estimation *IEE Proc.* F **140** 107–13
[26] van der Merwe R, Doucet A, de Freitas N and Wan E 2000 The unscented particle filter *Technical Report* CUED/F-INFENG/TR 380, Cambridge University, Engineering Department
[27] Douc R, Cappe O and Moulines E 2005 Comparison of resampling schemes for particle filtering *Proc. 4th Int. Symp. on Image and Signal Processing and Analysis (Zagreb, Croatia)* pp 64–9
[28] Watzenig D, Steiner G and Pröll C 2005 Statistical estimation of phase boundaries and material parameters in industrial process tomography *Proc. IEEE Int. Conf. on Industrial Technology (Hong Kong, China)* pp 720–5